Received: 12 January 2023 | Revised: 18 August 2023 | Accepted: 18 August 2023

DOI: 10.1002/mrm.29857

RESEARCH ARTICLE

Magnetic Resonance in Medicine

Effectiveness of visual biofeedback–guided respiratory-correlated 4D-MRI for radiotherapy guidance on the MR-linac

Katrinus Keijnemans | **Pim T. S. Borman** | **Bas W. Raaymakers** | **Martin F. Fast**

Department of Radiotherapy, University Medical Center Utrecht, Utrecht, The Netherlands

Correspondence
Katrinus Keijnemans, Department of Radiotherapy, University Medical Center Utrecht, Heidelberglaan 100, 3584 CX Utrecht, The Netherlands.
Email: k.keijnemans-2@umcutrecht.nl

Funding information
Nederlandse Organisatie voor Wetenschappelijk Onderzoek, Grant/Award Number: 17515

Abstract

Purpose: Respiratory-correlated 4D-MRI may provide motion characteristics for radiotherapy but is susceptible to irregular breathing. This study investigated the effectiveness of visual biofeedback (VBF) guidance for breathing regularization during 4D-MRI acquisitions on an MR-linac.

Methods: A simultaneous multislice-accelerated 4D-MRI sequence was interleaved with a one-dimensional respiratory navigator (1D-RNAV) in 10 healthy volunteers on a 1.5T Unity MR-linac (Elekta AB, Stockholm, Sweden). Volunteer-specific breathing amplitudes and periods were derived from the 1D-RNAV signal obtained during unguided 4D-MRI acquisitions. These were used for the guidance waveform, while the 1D-RNAV positions were overlayed as VBF. VBF effectiveness was quantified by calculating the change in coefficient of variation (CV^{diff}) for the breathing amplitude and period, the position SD of end-exhale, end-inhale and midposition locations, and the agreement between the 1D-RNAV signals and guidance waveforms. The 4D-MRI quality was assessed by quantifying amounts of missing data.

Results: VBF had an average latency of 520 ± 2 ms. VBF reduced median breathing variations by 18% to 35% (amplitude) and 29% to 57% (period). Median position SD reductions ranged from −3% to 35% (end-exhale), 29% to 38% (end-inhale), and 25% to 37% (midposition). Average differences between guidance waveforms and 1D-RNAV signals were 0.0 s (period) and +1.7 mm (amplitude). VBF also decreased the median amount of missing data by 11% and 29%.

Conclusion: A VBF system was successfully implemented, and all volunteers were able to adapt to the guidance waveform. VBF during 4D-MRI acquisitions drastically reduced breathing variability but had limited effect on missing data in respiratory-correlated 4D-MRI.

KEYWORDS

4D-MRI, abdominothoracic cancer, MR-linac, radiotherapy, visual biofeedback

1 | INTRODUCTION

It is important to perform motion management in the abdominal and thoracic regions during external beam radiotherapy, as the anatomy and tumor move because of respiration.[1–3] The current standard of care for quantifying respiratory-induced motion is 4D-CT for treatment planning[4–7] and 4D cone-beam CT (4D-CBCT) for position verification on a CT-linac.[8,9] MRI is used increasingly in radiotherapy for treatment simulation (MR simulation) and guidance (MR-linac).[10,11] In recent years, respiratory-correlated 4D-MRI has proven to be useful for guiding abdominothoracic radiotherapy on the MR-linac.[12,13] Nevertheless, natural variations in breathing cycles can affect the 4D-MRI quality, which in turn affects the motion estimation and delineation accuracy.

One way to aid 4D-MRI-based motion management is to provide breathing instructions during image acquisition and treatment, which can be displayed directly to the patient in the MRI bore using a projector, a monitor, or display goggles.[14–16] Providing visual biofeedback (VBF) to the patient on their respiratory anatomical motion can potentially increase motion regularity and reproducibility. A free-breathing 4D-MRI acquisition typically takes 3–5 min, with the respiratory-correlated 4D-MRI representing the average anatomical motion during this acquisition. Regularizing the breathing during the 4D-MRI acquisition improves the alignment between imaging and treatment, as the 4D-MRI more accurately represents the anatomical motion that can be used for an internal target volume (ITV) or a midposition (i.e., time-averaged position) treatment.[12]

A reduction in residual motion and an increase in breathing regularity and reproducibility as a result of VBF have been shown in several studies.[6,17–23] However, these studies used external motion surrogates (e.g., surface cameras, spirometers, thermocouples, pressure belts). These external surrogates do not always represent internal anatomical motion, which is the important property for radiotherapy.[24–26]

Internal navigators overcome this problem and require no additional sensing hardware when used for VBF. The standard approach to estimate internal anatomical motion is using a one-dimensional respiratory navigator (1D-RNAV).[27,28] Alternatively, visual guidance systems were implemented on the MRIdian MR-linac (Viewray Inc., Oakwood Village, OH, USA) that visualized the internal anatomy directly during respiratory-gated deliveries.[14,29,30] However, this requires cine images intersecting the target and is therefore not compatible with 4D-MRI. Instead of visualizing the internal anatomy directly, motion could also be estimated from the image data and shown as VBF. We previously developed a simultaneous multislice (SMS)-accelerated 4D-MRI sequence, in which respiratory-correlated 4D-MRIs are obtained by self-navigation (i.e., motion estimation from the actual image data)[30] using slice-based template matching (2D-RNAV).[31]

In this study, a novel internal navigator–based VBF system has been developed for the Unity MR-linac (Elekta AB, Stockholm, Sweden) and applied to a 4D-MRI acquisition protocol. The aims of the study were to evaluate the effects of VBF on respiratory motion and image quality during 4D-MRI acquisition, and to evaluate the fidelity of 1D-RNAV and 2D-RNAV signals.

2 | METHODS

The developed VBF setup is described in Section 2.1, and the data flow (1D-RNAV and imaging data) is described in Section 2.2. Latency experiments (Section 2.3) were performed to display the VBF with the correct delay relative to the guidance waveform. Several MRI acquisitions (Section 2.4) were performed to investigate the effects of VBF on respiratory motion (Section 2.5.1) and respiratory-correlated 4D-MRIs (Section 2.5.3). Finally, the 1D-RNAV signal validation with phantom data and in vivo data is described (Section 2.6).

Data were acquired on a 1.5T Unity MR-linac in 10 healthy volunteers (age 25–61 years, weight 59–76 kg, male: female 7:3). The study was approved by the local ethics committee, and all subjects provided written informed consent before participation.

2.1 | VBF system

A 1D-RNAV[28,32] was added to an SMS-4D-MRI sequence (details in Section 2.4.1) and acquired on the liver–lung interface before each pair of SMS slices (Figure 1A,B). The respiratory position (red indication, Figure 1C) was obtained by performing edge detection on the reconstructed 1D-RNAV data. The reconstructed 1D-RNAV data were smoothed with a median filter (window size = 5 voxels), and the (default host) threshold for edge detection was increased by 50% to prevent outlier edge detections. The 1D-RNAV position was displayed using a custom graphical user interface (GUI) on an MR-compatible monitor (Figure 1D,E). This monitor was located behind the MR-linac bore and visible through an MR-compatible mirror (Figure 1F). The GUI displayed the guidance waveform as a rolling waveform, while the most recent 1D-RNAV position was displayed at its acquisition time point, including correction for latency (Section 2.3).

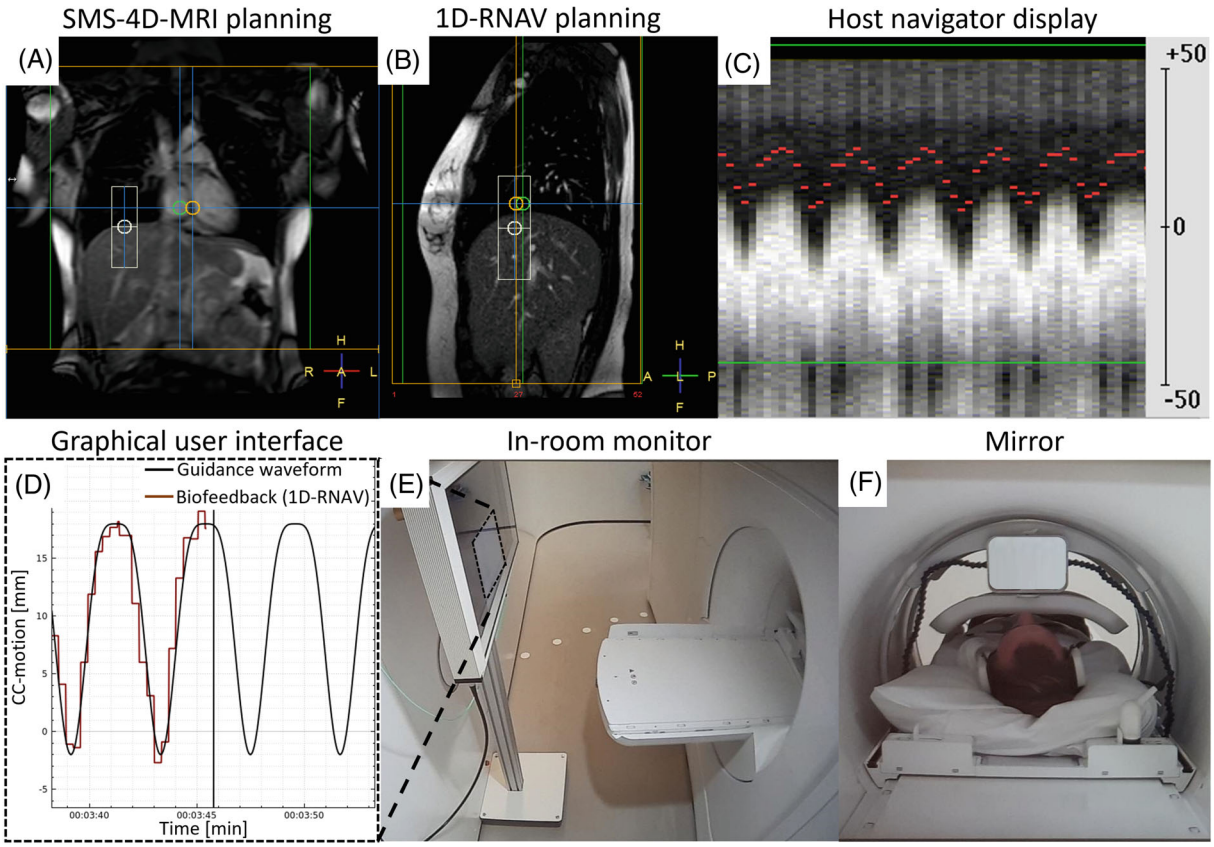

FIGURE 1 Visual biofeedback setup on the MR-linac: simultaneous multislice (SMS)-accelerated 4D-MRI FOV (orange box) (A); one-dimensional respiratory navigator (1D-RNAV) FOV (white box) on the liver–lung interface (B); acquired 1D-RNAV intensity profile columns and corresponding derived 1D-RNAV positions (red bars) (C); displayed guidance waveform (continuous line), respiratory position (discrete line), and current time point (vertical line) (D); MR-compatible monitor behind the bore (E); and MR-compatible mirror mounted on an arch (F).

2.2 | VBF data flow

Figure 2 shows the methodology of the 4D-MRI acquisition with VBF. SMS data and 1D-RNAV data were acquired on the MR-linac. The 1D-RNAV-derived position was sent as metadata along with the acquired SMS data to the host reconstructor. The 1D-RNAV (Section 2.2.1) and image (Section 2.2.2) data were streamed to a message broker using ReconSocket,[33] which is an in-house-developed library that was added as a module to the scanner reconstruction framework.

2.2.1 | One-dimensional RNAV data flow

When received in the host reconstructor, the acquired SMS data with the 1D-RNAV position were streamed directly (without processing) to a message broker. From here, the data were saved to disk with a timestamp using a client program and sent to a program where the 1D-RNAV position was extracted from the metadata. This program featured a GUI that was used to display the 1D-RNAV position as VBF and the guidance waveform to be followed on an in-room monitor. The displayed positions were saved every 20 ms with a timestamp for further analysis.

2.2.2 | Four-dimensional MRI data

In parallel with the 1D-RNAV data flow, the pair of SMS images was reconstructed on the scanner and then sent to the message broker. Here, a client program timestamped and saved the SMS images to disk. These images were then sorted offline into respiratory-correlated 4D-MRIs using either the stored 1D-RNAV positions or using the 2D-RNAV intrinsic to the 4D-MRI sequence (Section 2.6.1).

2.3 | Latency measurement

The VBF system includes a latency between acquiring and displaying the VBF, which was determined with the Quasar MRI^{4D} phantom (Modus Medical Devices Inc.,

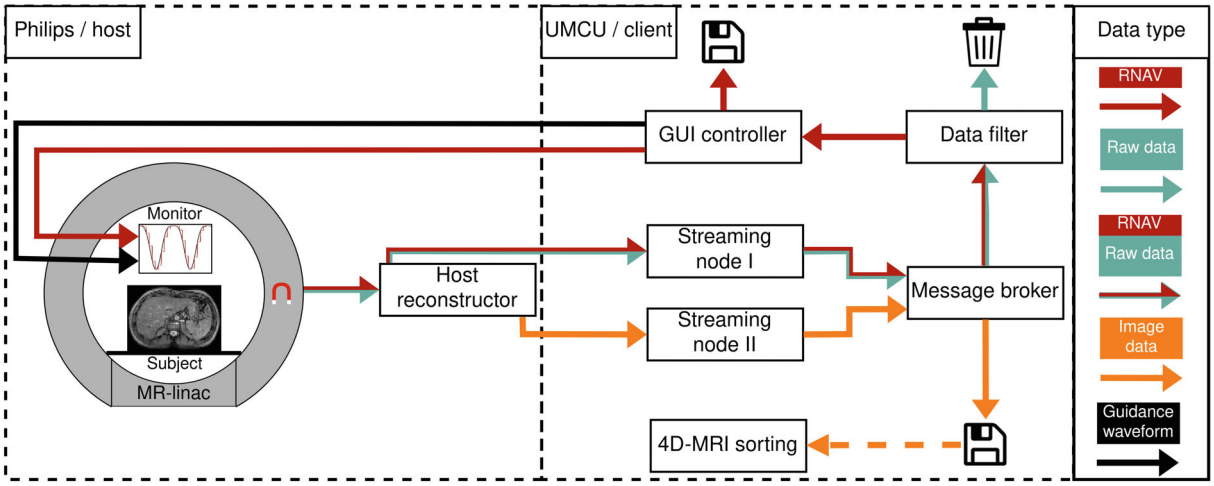

FIGURE 2 Schematic overview of the data flow. Acquired image data and one-dimensional respiratory navigator (1D-RNAV) position at the MR-linac are sent to the host reconstructor. Acquired image data with the 1D-RNAV position were sent directly through the ReconSocket module (Streaming Node I) to a message broker and then sent to a program (data filter) that extracted the 1D-RNAV position. The 1D-RNAV position was then displayed with a guidance waveform on an in-room monitor using a graphical user interface (GUI). Reconstructed image data were sent through the ReconSocket module (Streaming Node II) to a message broker and then saved to disk for further offline respiratory-correlated 4D-MRI sorting.

London, ON, Canada) to correct for it. The phantom was programmed to follow a sinusoidal trajectory ($A = 20$ mm, $T = 4$ s) while data were acquired. The phantom reported positions were timestamped and stored in a log file every 25 ms by a client program, as were the displayed positions (every 20 ms) on the monitor (Section 2.2.1). The minimum latency (τ_{minimum}) consisted of the three components, as follows:

$$\tau_{\text{minimum}} = \frac{T_{\text{RNAV}}}{2} + T_{\text{image}} + T_{\text{proc}} \quad (1)$$

where T_{RNAV} is the 1D-RNAV acquisition time; T_{image} is the image acquisition time; and T_{proc} is the processing time that consisted of extracting the 1D-RNAV position and displaying this position. Half of T_{RNAV} contributed due to the signal being effectively measured halfway, while T_{image} contributed to τ_{minimum}, because the 1D-RNAV position was sent along with the imaging data. The value of τ_{minimum} was determined by calculating the phase shift between the pre-programmed sinusoidal waveform and the displayed 1D-RNAV positions.[34] The frequency of updating the displayed 1D-RNAV positions was limited by the acquisition time of the RNAV itself and the pair of SMS images. Therefore, adding half of the T_{RNAV} and T_{image} to the minimum latency yields the average latency (τ_{average}), as follows:

$$\tau_{\text{average}} = \tau_{\text{minimum}} + \frac{T_{\text{RNAV}} + T_{\text{image}}}{2} \quad (2)$$

where typically $T_{\text{RNAV}} \ll T_{\text{image}}$.

2.4 | Four-dimensional MRI acquisitions

Eight 4D-MRI acquisitions were performed per volunteer during free-breathing. An unguided acquisition (Section 2.4.2) was performed that served as reference, which was followed by three guided acquisitions (Section 2.4.3). In the first session, the feasibility of VBF and adaptability of volunteers was tested, and a second acquisition session was performed as consistency check and to determine whether volunteers were able to maintain regular breathing for over half an hour.

2.4.1 | Four-dimensional MRI sequence

A single-shot T_2-weighted SMS-accelerated turbo spin echo (TSE) 4D-MRI sequence was repeatedly acquired and interleaved with the 1D-RNAV acquisition. This 4D-MRI sequence acquires two coronal slices simultaneously, and repeatedly acquires slices over the image volume covering a stack of 52 slices per repetition (hereafter "dynamic") with the following parameters: FOV = 457×208–260×350 mm^3 in respectively left–right (LR), anteroposterior (AP), and craniocaudal (CC) directions, in-plane resolution = 2×2.5 mm^2, 4–5 mm slice thickness, 0-mm slice gap, 2.5 in-plane acceleration, 0.625 partial Fourier factor, 110° flip angle (FA), 57-ms TE, 318-ms slice acquisition time, 8908-ms TR, and interleaved slice order. The 1D-RNAV acquisition had the following parameters: FOV = 30 (LR) × 30 (AP) × 100 (CC) mm^3

(cylindrical), 1-mm resolution, 20° FA, and 25-ms acquisition time.

2.4.2 | Unguided acquisition

The first SMS-4D-MRI was acquired in free-breathing without VBF for 30 dynamics (4:27 min:s). The concurrently obtained 1D-RNAV positions were used to extract the average peak-to-peak amplitude (hereafter "amplitude", A) and period (T) that represented the subject-specific natural breathing. The guidance waveform was modeled as a $A * \cos^4\left(\frac{\pi * t}{T}\right)$ waveform using the derived A and T, which were used during the experiments with VBF.[35]

2.4.3 | Guided acquisitions

Session 1

The first guided 4D-MRI acquisition (35 dynamics, 5:12 min:s) had a guidance waveform with the amplitude and period derived from the unguided acquisition, to investigate whether volunteers were able to breath regularly. In the second guided acquisition (35 dynamics, 5:12 min:s), the period of the guidance waveform was increased by 50%. Here we investigated how well volunteers were able to adjust their breathing to deviate from natural breathing. The third guided acquisition (70 dynamics, 10:24 min:s) was a longer acquisition, again using subject-specific amplitude and period. Here, we investigated the ability of volunteers to maintain regular breathing for a longer total time. The first five dynamics of data acquired during guided acquisitions were discarded for analyses, as volunteers had to adjust their breathing to the guidance waveform. The long acquisition resulted in 65 dynamics of data for analyses. Using a sliding window approach with 30 dynamics of data per 4D-MRI reconstruction resulted in 36 respiratory-correlated 4D-MRIs.

Session 2

In the second session performed on a different day, three acquisitions of 75 dynamics (11:09 min:s) were performed with guidance, using the amplitude and period derived from the unguided acquisition of this session. The first two dynamics of data of each acquisition were discarded for analyses, resulting in 219 dynamics of data for analyses. Despite an approximate 1-min gap between the scans, they were analyzed as one long acquisition by concatenating end-inhale locations. Using the sliding window approach, a total of 190 4D-MRIs were sorted. For Volunteer 5, 184 dynamics of data were acquired.

2.5 | Effects of VBF guidance

2.5.1 | Respiratory motion

The coefficient of variation (CV), which is defined as the ratio between the SD and the mean, was determined as a measure of variability for the amplitude and period (Eq. [3]). The 1D-RNAV motion traces were split into individual breathing cycles by detecting the end-inhale locations and used to determine the SD and mean for the amplitude and period. Values outside the 2.5th to 97.5th percentile range were excluded as outliers. The percentage difference in variation with respect to the unguided acquisition was determined as described in Eq. (4), and systematic offsets during guidance (i.e., the difference between μ_{Unguided} and the guidance waveform) were compensated for. A decrease in variability will be reflected by a negative CV^{diff}.

$$\text{CV}_{\text{a,b}} = \frac{\sigma_{\text{a,b}}}{\mu_{\text{a,b}}} \tag{3}$$

$$\text{CV}^{\text{diff}}_{\text{b}}\,[\%] = \frac{\text{CV}_{\text{Guided,b}} - \text{CV}_{\text{Unguided,b}}}{\text{CV}_{\text{Unguided,b}}} * 100\% \tag{4}$$

where a ∈ {Unguided, Guided}, b ∈ {Amplitude, Period}.

The variation in end-exhale, end-inhale, and midposition locations was quantified by calculating the SD of the positions in the individual breathing cycles for each 4D-MRI data set. A smaller SD will be found if breathing is consistent and in the absence of baseline drift in the respiratory waveform. Baseline drift was quantified in the long acquisition, as the difference in midposition compared with the first 4D-MRI subset. Brown–Forsythe tests were performed to establish a statistically significant difference in the variances of the end-exhale, end-inhale, and midposition distributions between unguided and guided acquisitions ($p < 0.05$).

2.5.2 | VBF compliance

The VBF performance was determined by calculating the mean and SD in the difference of the amplitudes and periods in the individual breathing cycles of the 1D-RNAV signals, compared with the programmed guidance waveforms.

2.5.3 | Respiratory-correlated 4D-MRI

Respiratory-correlated 4D-MRI reconstruction

Respiratory-correlated 4D-MRIs were sorted using the obtained 1D-RNAV positions. The 1D-RNAV signals were

linearly interpolated to match the image acquisition time points, which then represented the navigation signal to sort the 4D-MRIs. A data inclusion range of 95%, which minimized the amplitude, was implemented to exclude outlier motion and minimize missing data in the sorted 4D-MRIs. The image data were sorted based on amplitude binning with 10 respiratory bins (phases) that accounted for hysteresis.[31]

Missing data and clustering in 4D-MRI

The sorting of the 4D-MRI can be represented as filling a 2D location-phase matrix (slice location vs. respiratory phase) based on all acquired dynamics. Missing data in the 2D location-phase matrix were estimated by applying linear interpolation of neighboring slices and respiratory phases.[31] The amount of missing data and clustering of missing data were quantified to determine the quality of the sorted 4D-MRI. The total amount of missing data was divided into two categories: missing entries with a maximum of one missing neighbor, and missing entries with two or more missing neighbors in the 2D location-phase matrix. Resolving missing data with linear interpolation for this latter category typically results in lower quality missing data estimation. Clusters of missing data were identified by detecting the four-point neighbors of missing data in the location-phase matrix of the 4D-MRI, and the largest cluster was quantified.

Liver–lung interface smoothness

To validate the liver–lung interface smoothness in the AP direction of the respiratory-correlated 4D-MRIs, a sagittal balanced turbo-field-echo 2D-cine MRI sequence was acquired with the following parameters: FOV = 245 (AP) × 350 (CC) mm^2, in-plane resolution = 1.5 × 1.5 mm^2, 10 mm slice thickness, 2.0 in-plane acceleration, 50° FA, 1.8-ms TE, 3.7-ms TR, 302-ms slice acquisition time, and 90 dynamics. The sagittal 2D-cine MRI was used to determine the root mean square error (RMSE) between the reconstructed liver–lung interface in the sorted 4D-MRIs and this ground-truth scan. This RMSE was compared to the missing data percentage to quantify the sorted 4D-MRI quality, as incorrectly sorted data decreases the missing data percentage, but increases the RMSE.

2.6 | RNAV validation

2.6.1 | Estimating the 2D-RNAV surrogate signal

Self-navigation was performed using template matching (normalized cross-correlation) in a region of interest at the liver–lung interface to obtain a 2D-RNAV.[31] The self-navigation approach uses the central half of the image stack (called navigator slices) for sorting. After registering the navigator slices to an intrinsic reference volume, a 4D motion model is used to account for nonuniform CC motion of the liver across the AP slice locations,[31,36] yielding the 2D-RNAV surrogate signal. The 1D-RNAV was acquired at a constant location at the liver–lung interface before the acquisition of each pair of SMS images. Therefore, the acquired images at the location of the 1D-RNAV acquisition were visually assessed for signal interference (loss of signal), which could degrade image quality and thus the 2D-RNAV.

2.6.2 | One-dimensional RNAV versus 2D-RNAV

In vivo

An additional acquisition of a single pair of SMS images was performed during the first session, when one of the two slices was acquired at the 1D-RNAV location. These data were used to cross-validate the in vivo agreement between respiratory motion obtained from the 1D-RNAV and from self-navigation in the SMS images (2D-RNAV). For this acquisition, a single-shot T_2/T_1-weighted SMS-accelerated balanced turbo-field-echo sequence was used with the following parameters: 5-mm slice thickness, 1.5 in-plane acceleration, 60° FA, 2.8-ms TE, 5.5-ms TR, 492-ms slice-acquisition time, 75 dynamics, and 130-mm slice separation. Other parameters matched the TSE-4D-MRI parameters (Section 2.4.1).

The interpolated 1D-RNAV (to match image acquisition time points) and 2D-RNAV surrogate signals were compared using both RMS deviation (RMSD) and Pearson correlation for both 4D-MRI and two-slice SMS acquisitions. Furthermore, the amplitudes were derived from the surrogate signals and compared with each other for the 4D-MRI acquisitions.

Phantom data

The Quasar MRI^{4D} motion phantom was used for validation of the 1D-RNAV and 2D-RNAV signals. A cylindrical insert filled with agar gel was placed in the peripheral insert location. The phantom was programmed with sinusoidal waveforms with amplitudes of 20, 25, and 30 mm and periods of 4.0, 4.3, and 4.6 s. The SMS-TSE acquisition was performed with the 1D-RNAV acquired at the cranial side of the insert, representing the lung–liver transition. The image stack was reduced to 28 slices with a 4-mm slice thickness (FOV = 457 × 112 × 350 mm^3) to match the cylinder dimensions. The 1D-RNAV FA was increased to 60° while other scan parameters matched the in vivo settings. Consistent with the in vivo data, the

image quality at the location of the 1D-RNAV acquisition was visually assessed to determine signal interference, and 2D-RNAV signals were derived from the acquired phantom images. The differences between the amplitudes in the RNAV signals and the ground-truth motion of the phantom were evaluated, and the RNAV signals were compared with each other using the Pearson correlation and RMSD.

2.6.3 | 2D-RNAV 4D-MRI reconstructions

Respiratory-correlated 4D-MRIs were sorted as described in Section 2.5.3 using the 2D-RNAV surrogate signals (instead of 1D-RNAV), and the amount of missing data and clustering were quantified. A two-sided Wilcoxon rank sum test ($p < 0.05$) was performed to compare the difference in missing data percentage obtained with the 1D-RNAV and 2D-RNAV. A comparison was made for the unguided and guided acquisitions in one session, and between the two sessions. Additionally, the liver–lung interface smoothness was quantified by calculating the RMSE compared with the ground-truth sagittal 2D-cine MRI.

3 | RESULTS

3.1 | Latency of the VBF system

The minimum (τ_{minimum}) and average (τ_{average}) latencies were measured to be 356 ± 4 ms and 520 ± 2 ms, respectively. Each 1D-RNAV position was shown to the subjects with a τ_{minimum} offset relative to the guidance waveform.

3.2 | VBF effects

3.2.1 | Respiratory motion

Figure 3 shows the $CV^{diff}_{Amplitude}$ and CV^{diff}_{Period}, and Table 1 summarizes these values with their underlying changes in mean and SD. Over all volunteers, the $CV^{diff}_{Amplitude}$ was between −35% and −18%, whereas the CV^{diff}_{Period} was between −57% and −29%. An increase in mean ($\Delta\mu$) was found for the $CV^{diff}_{Amplitude}$, whereas the decrease in SD ($\Delta\sigma$) was larger. The CV^{diff}_{Period} was primarily a result of a decreased SD.

An increased amplitude variability (i.e., a positive $CV^{diff}_{Amplitude}$) was observed in Volunteers 2 and 5 (long

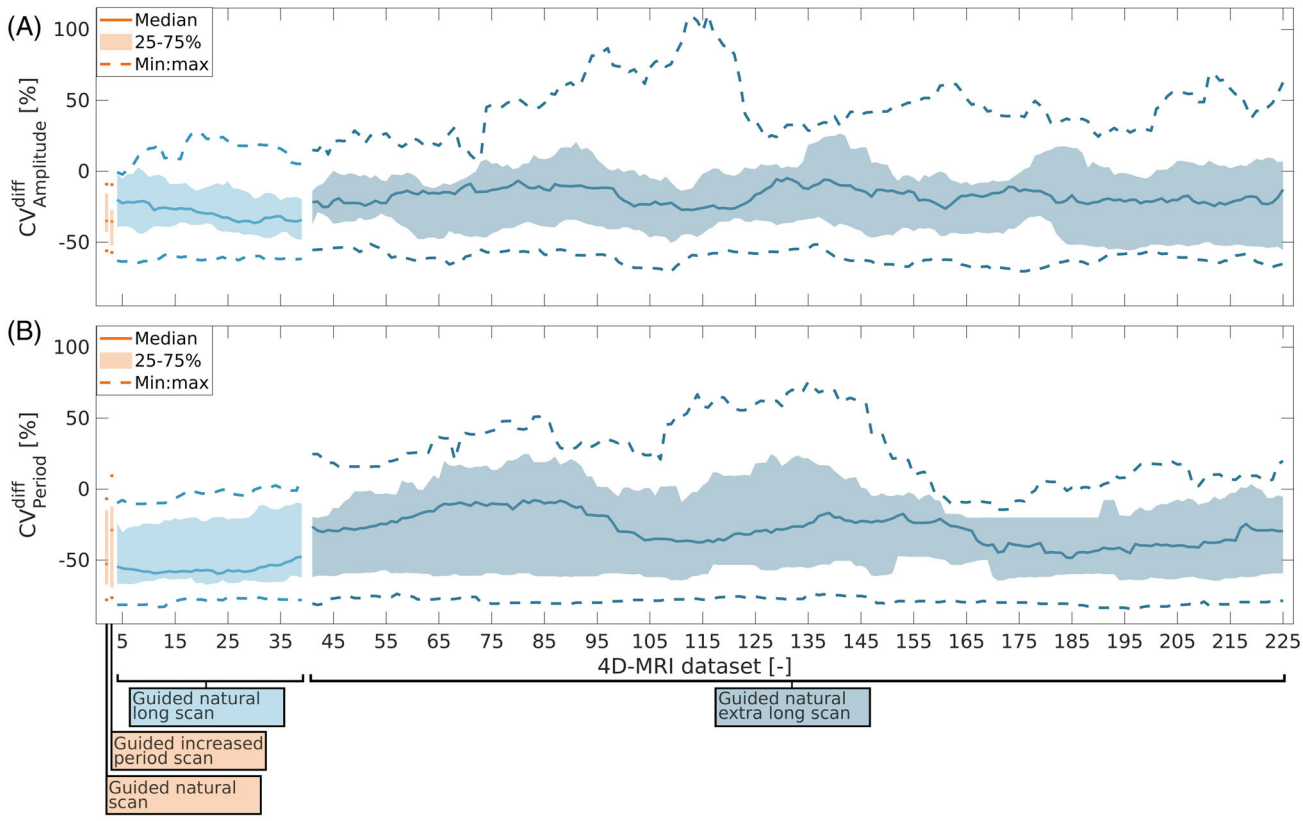

FIGURE 3 The percentage difference in coefficient of variation (CV^{diff}) between acquisitions with visual biofeedback and the unguided 4D-MRI acquisition for the peak-to-peak amplitude (A) and period (B). Data Sets 2 and 3 represent the natural guided and guided with 50% increased period acquisitions, respectively, whereas Data Sets 4–39 are derived from the long-guided acquisition of the first session. Data Sets 41–225 were acquired during the extra-long acquisition in the second session. Unguided Acquisitions 1 and 40 were used as references.

TABLE 1 Median (min:max) percentages of the difference in coefficient of variation (CV^{diff}) for the peak-to-peak amplitude and period, and the corresponding change in mean ($\Delta\mu$) and SD ($\Delta\sigma$).

	Amplitude			Period		
	CV^{diff} (%)	$\Delta\sigma$ (%)	$\Delta\mu$ (%)	CV^{diff} (%)	$\Delta\sigma$ (%)	$\Delta\mu$ (%)
Guided natural	−35 (−56:−9)	−14 (−46:29)	10 (4:63)	−53 (−78:−7)	−52 (−78:−6)	1 (1:4)
Guided increased period	−35 (−57:−9)	−24 (−53:9)	20 (9:50)	−29 (−77:9)	−28 (−76:11)	1 (−1:1)
Guided natural long	−30 (−65:28)	−21 (−57:64)	15 (−8:37)	−57 (−83:9)	−57 (−83:9)	1 (0:2)
Guided natural extra long	−18 (−71:111)	−9 (−66:97)	9 (−17:35)	−31 (−84:76)	−29 (−84:79)	1 (−2:5)

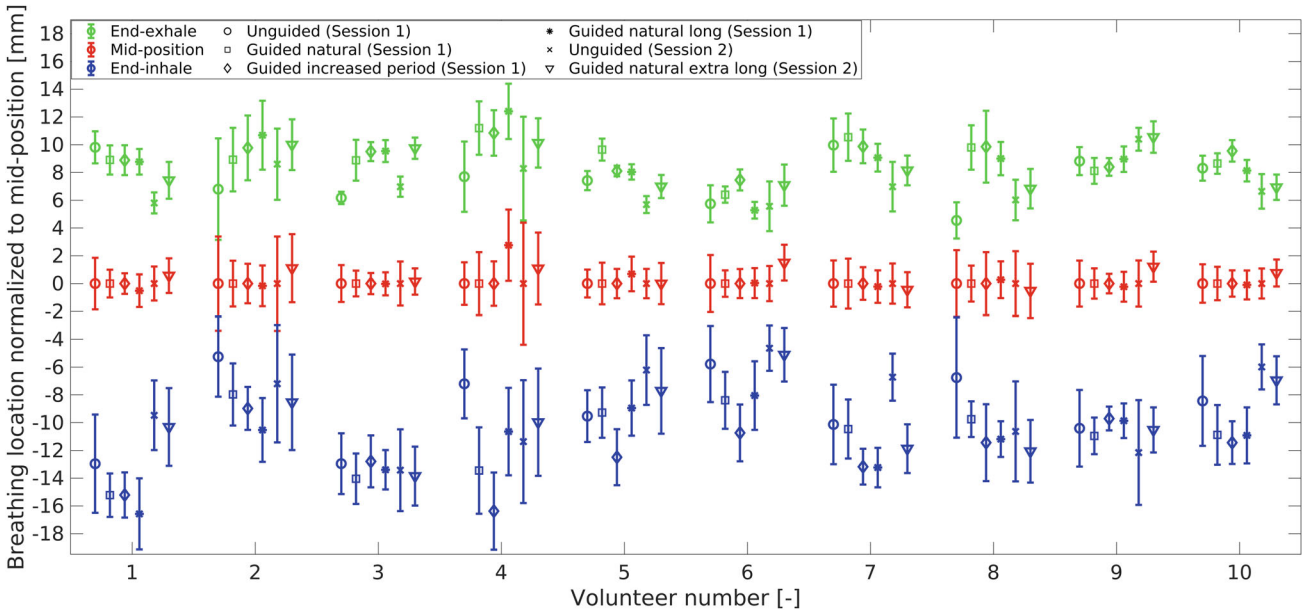

FIGURE 4 One-dimensional navigator median position and SD for end-exhale (top), midposition (i.e., time-averaged position, middle), and end-inhale (bottom) locations. Guidance reduced the position SD, and midposition locations were stable during the long acquisitions.

TABLE 2 Median (min:max) values of the position SD of end-exhale, end-inhale, and midposition locations.

	End-exhale			End-inhale			Midposition		
		BF $p < 0.05$ (%)			BF $p < 0.05$ (%)			BF $p < 0.05$ (%)	
Scan	SD (mm)	Decrease	Increase	SD (mm)	Decrease	Increase	SD (mm)	Decrease	Increase
1	1.2 (0.4:3.7)	–	–	2.8 (1.9:4.3)	–	–	1.7 (1.0:3.4)	–	–
2	1.3 (0.6:2.3)	30	10	1.9 (1.3:3.1)	60	10	1.2 (0.9:2.3)	60	20
3	0.9 (0.4:2.6)	50	10	1.7 (0.9:2.8)	60	0	1.1 (0.7:2.3)	60	0
4	0.9 (0.5:2.8)	29	8	1.9 (0.9:3.0)	49	5	1.2 (0.7:2.6)	63	9
5	1.4 (0.6:2.7)	–	–	2.7 (1.6:4.4)	–	–	1.5 (1.1:4.4)	–	–
6	0.9 (0.3:2.2)	66	4	1.9 (0.9:5.6)	43	5	1.1 (0.5:3.0)	64	2

Note: For the Brown-Forsythe tests, the percentage of statistically significant tests ($p < 0.05$) corresponding to a decrease or an increase in variance is summarized. Scans 1 (unguided), 2 (guided natural), 3 (guided increased period), and 4 (guided natural long) belong to Session 1, and Scans 5 (unguided) and 6 (guided natural extra-long) belong to Session 2.
Abbreviation: BF, Brown-Forsythe.

acquisition) and in Volunteer 4 (extra-long acquisition). The latter determined 74% of the maximum line in Figure 3A. For Volunteer 6, the amplitude variability showed an improvement that gradually decreased as the $CV^{diff}_{Amplitude}$ increased from −32% to −2%. Although Volunteers 4, 5, and 7 had reduced breathing period

variability during the long acquisition, their negative CV^{diff}_{Period} increased over time by 29%, 14%, and 18%, respectively. However, during the extra-long acquisition, Volunteers 5, 6, and 8 were not able to maintain the instructed regular breathing, resulting in a positive CV^{diff}_{Period}.

Figure 4 shows the median and SD of the end-exhale, midposition, and end-inhale locations in CC direction normalized by the midposition location as determined from the 1D-RNAV surrogate signal. Table 2 summarizes the position SD and the percentages of statistically significant variance tests. For the first guided scan, the median end-exhale position SD increased by 3% from 1.2 mm to 1.3 mm. For the other guided scans, the median position SD decreased by 25% to 35%. A significant decrease in the variance of end-exhale locations was found in 29% to 66% of the data sets. The 8% and 10% of significant increases in variance during the first session corresponded only to Volunteer 3. Regarding the end-inhale locations, VBF decreased the median position SD by 29% to 38%. A significant difference in variance was found in 43% to 60% (decrease) and 0% to 10% (increase) of the data sets, the latter corresponding to Volunteer 4. For the midposition anatomy, VBF decreased the median position SD by 25% to 37%, and the variance was statistically significantly reduced in 60% to 64% of the data sets. The median (min:max) absolute drifts were 0.2 (0.0:3.3) mm and 0.8 (0.0:5.5) mm for the long and extra-long acquisitions, respectively.

3.2.2 | VBF compliance

The mean (SD) differences between the end-exhale locations in the 1D-RNAV signal and guidance waveform were 2.2 (1.6) mm, 2.3 (1.3) mm, 1.9 (1.7) mm, and 1.7 (0.9) mm for the guided natural, guided increased period, guided natural long, and the guided natural extra-long acquisitions, respectively. For the end-inhale locations, the differences were 0.3 (1.8) mm, −0.8 (1.4) mm, 0.4 (1.4) mm, and 1.5 (1.8) mm, respectively. These differences indicate an increase in amplitude, which was on average 1.7 mm. Compared with the guidance waveforms, the breathing periods in the 1D-RNAV signals had a mean (SD) error of 0.1 (0.5) s, 0.0 (0.5) s, 0.0 (0.3) s, and 0.1 (0.4) s for the four acquisitions with VBF, respectively.

3.2.3 | Respiratory-correlated 4D-MRI

Figure 5 shows the end-exhale and end-inhale respiratory phases of an exemplary guided 4D-MRI with the cylindrical 1D-RNAV acquisition location overlayed.

Missing data and clustering

Figure 6A shows the missing data percentage in the 4D-MRIs sorted using the 1D-RNAV. For the first session, a median (min:max) total missing data percentage of 3.8 (1.5:7.3)% was found for the unguided acquisition, which was reduced by 11% to a median (min:max) missing data

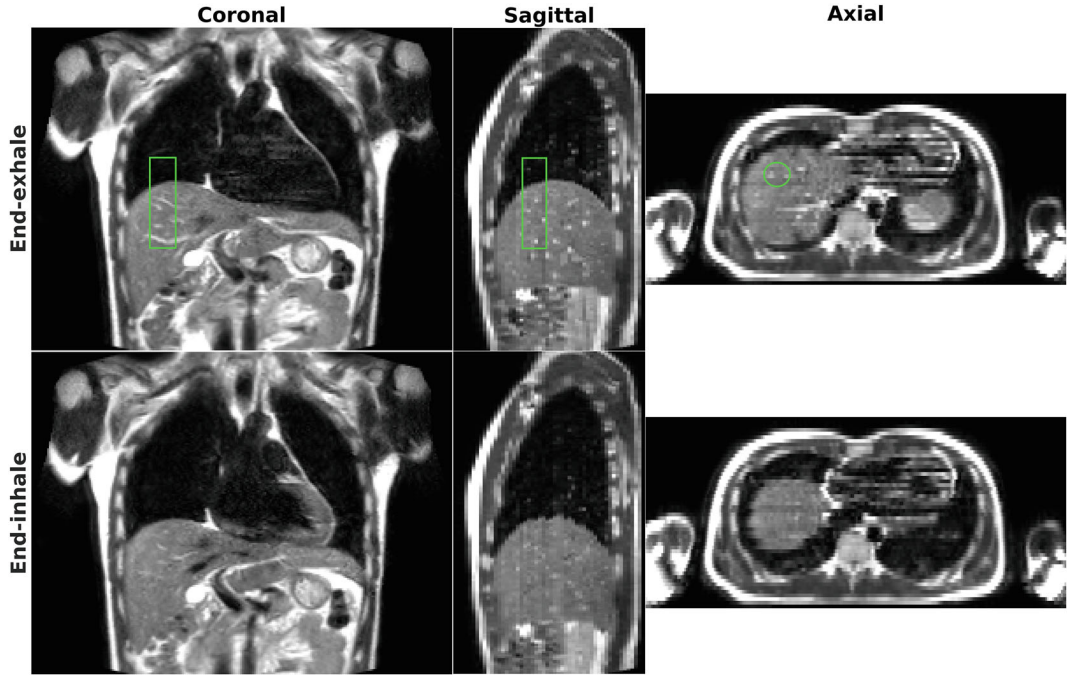

FIGURE 5 Example end-exhale and end-inhale respiratory phases of a sorted 4D-MRI acquired during guidance (Volunteer 10). The green volume represents the cylindrical one-dimensional respiratory navigator acquisition location.

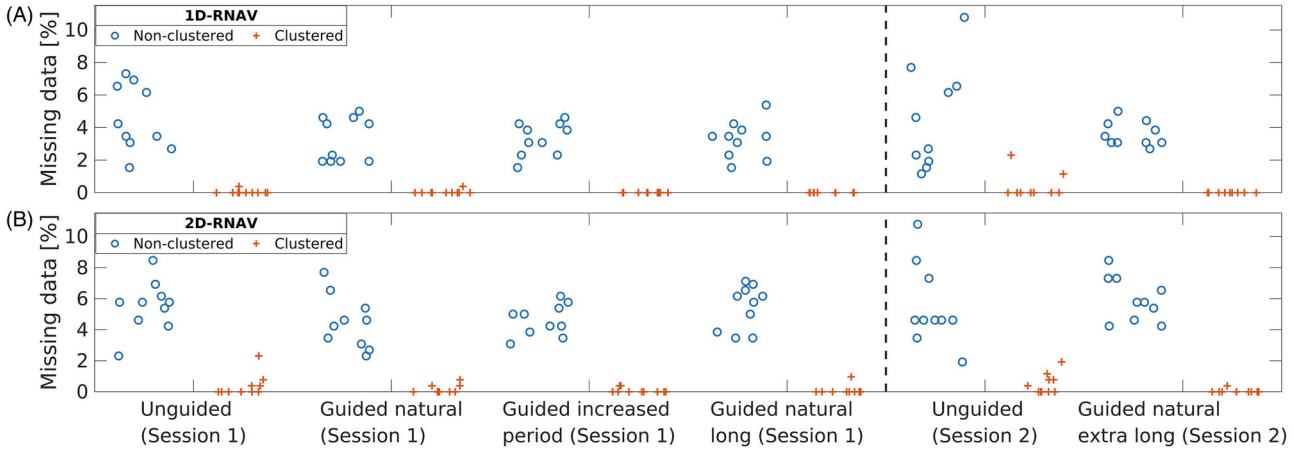

FIGURE 6 Missing data percentage in 4D-MRIs sorted using the one-dimensional respiratory navigator (1D-RNAV) (A) and the 2D-RNAV (B) of 10 volunteers for two imaging sessions. For the two long acquisitions, the median over 36 and 190 data sets is shown. Clustered missing data represent a missing slice location in a respiratory phase with two or more direct missing neighbors in slice location and/or respiratory phase.

percentage of 3.5 (0.4:8.5)% during acquisitions with VBF. The largest clustered missing data percentages were 0.4% (unguided) and 1.9% (guided).

In the second session, VBF reduced the median (min:max) total missing data percentage by 29% from 4.2 (1.2:10.8)% to 3.3 (2.7:5.0)%. The largest clustered missing data percentages were 1.2% (unguided) and 2.7% (guided).

Liver–lung interface smoothness

Figure 7 shows the liver–lung interface smoothness compared with the total missing data percentage. For the 4D-MRIs sorted using the 1D-RNAV signal, a median (min:max) RMSE of 1.1 (0.9:1.4) mm was found for the unguided and 1.2 (0.8:2.2) mm for the guided acquisitions in Session 1, corresponding to an 11% increase. The extra-long acquisition revealed a median (min:max) RMSE of 1.1 (0.8:1.7) mm and 1.4 (0.8:2.6) mm for the unguided and guided acquisitions, respectively, which is a 25% increase.

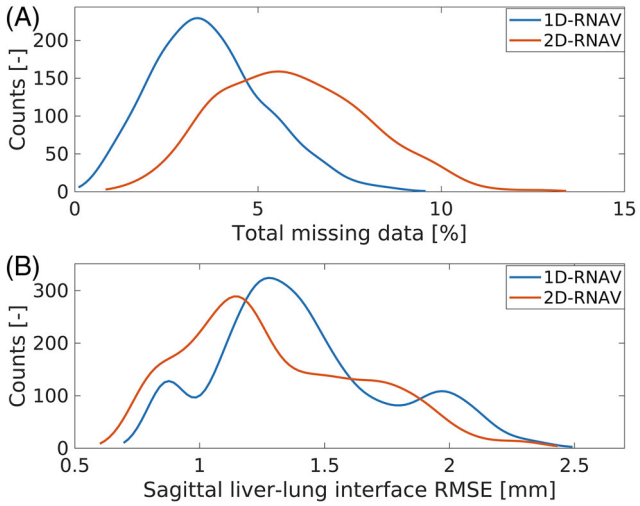

FIGURE 7 Distributions of the amount of missing data (A) and the liver–lung interface smoothness (B) in the respiratory-correlated 4D-MRIs. For the liver–lung interface smoothness, the median RMS error (RMSE) over the 10 respiratory phases is shown.

3.3 | RNAV validation

3.3.1 | Image-navigator signal interference

A visual inspection of the in vivo 4D-MRI data revealed no signal interference at the acquisition location of the 1D-RNAV. Conversely, however, the 1D-RNAV signal was affected by the 4D-MRI signal, resulting in a decreased SNR (Figure 1C). Fortunately, this effect was relatively mild and did not affect the usability of the 1D-RNAV for VBF. For the phantom acquisitions, mild signal interference in the images was observed, whereas the 1D-RNAV signal did not degrade.

3.3.2 | One-dimensional RNAV and 2D-RNAV agreement

In vivo data

For the two-slice SMS acquisition, a median (min:max) RMSD of 1.7 (1.1:2.6) mm was found between the 1D-RNAV and 2D-RNAV positions. The median (min:max) Pearson correlation was 0.95 (0.88:0.98).

Figure 8 shows the agreement of the 1D-RNAV and 2D-RNAV surrogate signals in terms of RMSD and their derived median amplitude per sorted 4D-MRI. A median (min:max) RMSD of 2.0 (1.1:3.9) mm was found between

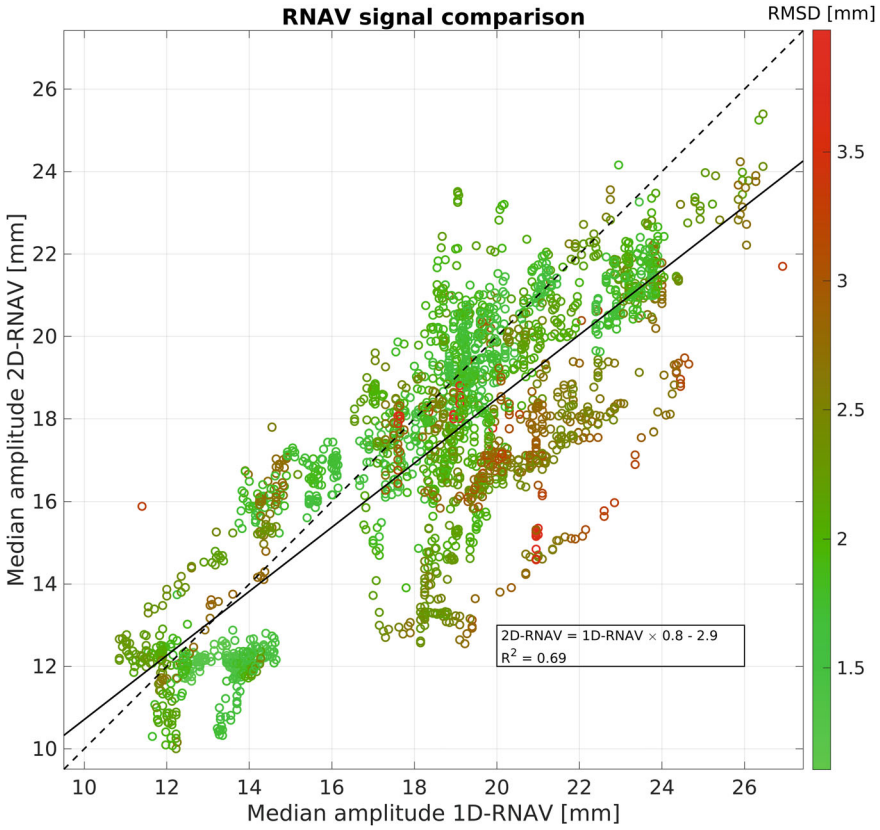

FIGURE 8 The root mean square deviation (RMSD) between the one-dimensional respiratory navigator (1D-RNAV) and 2D-RNAV surrogate signals was determined (color indication) for each 4D-MRI set ($N = 230$) of each volunteer ($N = 10$). For both signals, the median peak-to-peak amplitude per 4D-MRI set was determined, and a linear fit was performed (solid line).

the two surrogate signals with a median (min:max) Pearson correlation of 0.97 (0.81:0.99). The 2D-RNAV signal yielded a smaller amplitude (20%) compared with the 1D-RNAV signal. The linear fit between them had an R-squared of 0.69.

Phantom data

Compared with programmed peak-to-peak phantom motion, mean (SD) percentage differences of −3.0 (1.2)% and −2.1 (1.6)% were found for the 1D-RNAV and 2D-RNAV surrogate signals, respectively. The 1D-RNAV and 2D-RNAV surrogate signals had a Pearson correlation of 0.99 and a mean (SD) RMSD of 1.4 (0.3) mm for the phantom data.

3.3.3 | Two-dimensional RNAV 4D-MRI agreement

Figure 6B shows the missing data percentage in the obtained respiratory-correlated 4D-MRIs using the 2D-RNAV. For the unguided acquisitions, median (min:max) total percentages of 6.2 (2.3:8.5)% and 4.8 (1.9:12.7)% were found for the first and second session, respectively. The corresponding acquisitions with VBF had median (min:max) percentages of 5.4 (1.2:11.9)% and 5.8 (0.4:15.0)%. The largest clustered missing data percentages (two or more missing neighbors) were 2.3% (unguided Session 1), 0.8% (unguided Session 2), 2.3% (guided Session 1), and 2.7% (guided Session 2). For the liver–lung interface smoothness of the 2D-RNAV derived 4D-MRIs, a median (min:max) RMSE of 1.1 (0.7:2.4) mm and 1.2 (0.7:2.6) mm were found for unguided and guided acquisitions, respectively (Figure 7).

The difference in missing data percentage between the 1D-RNAV-sorted and 2D-RNAV-sorted 4D-MRIs was not statistically different for the unguided acquisitions in the first ($p = 0.21$) and second ($p = 0.54$) session. For the guided acquisitions in both sessions, the differences in missing data percentage between the 1D-RNAV-sorted and 2D-RNAV-sorted 4D-MRIs were found to be significant ($p < 0.001$). The difference in missing data percentage between the two sessions was not statistically significant for the unguided acquisitions ($p = 0.68$ for 1D-RNAV and $p = 0.57$ for 2D-RNAV). However, the differences were significant for the guided acquisitions: $p = 0.005$ for 1D-RNAV and $p < 0.001$ for 2D-RNAV.

4 | DISCUSSION

A VBF-guided 4D-MRI acquisition was successfully implemented on the Unity MR-linac by acquiring a 1D-RNAV interleaved with an SMS-accelerated 4D-MRI sequence

and displaying the derived 1D-RNAV position as VBF. The methodology demonstrated its ability to reduce median variability in breathing amplitudes by 18% to 35% and periods by 29% to 57%. Moreover, VBF increased the median stability of end-exhale locations by −3% to 35%, end-inhale locations by 29% to 38%, and midposition locations by 25% to 37%. This improved breathing regularity resulted in a reduction of 11% (Session 1) and 29% (Session 2) of missing data in the respiratory-correlated 4D-MRIs, while the liver–lung interface smoothness decreased by 11% (Session 1) and 25% (Session 2), which can be considered as minimum effects. The amount of missing data for the VBF guided acquisition was found to be significantly lower for the 1D-RNAV-sorted 4D-MRI compared with the 2D-RNAV-sorted 4D-MRI.

A 1D-RNAV acquisition was added to our SMS-4D-MRI sequence to obtain a physiological plausible surrogate for VBF to regularize breathing. The derived respiratory position was sent along with the SMS image data, introducing an additional latency caused primarily by the SMS acquisition time. If the 1D-RNAV position could be sent directly after its acquisition, the minimum latency would be limited to approximately 50 ms (streaming, extracting, and displaying the 1D-RNAV position) compared with the 356 ms in this work. However, the average latency would still be about 222 ms (Eq. [2]) based on the imaging frequency used in this study. Our volunteers reported no issues relating to latency. As a result of interleaving the RNAV and image acquisitions, the VBF was shown as a horizontal line for 343 ms (TR) until the next update, while the guidance waveform was updated every 20 ms. This VBF update frequency limitation applies to internal derived surrogate signals. A solution could be to use a predictor to predict subinterval respiratory positions.[20]

No signal loss was observed in the in vivo images at the 1D-RNAV navigator location, but the acquired 1D-RNAV signal had signal interference, which is reflected by the signal intensities acquired in the lung and loss of signal in the liver shown in Figure 1C. Despite this distortion, accurate motion was extracted with the implemented median filtering and threshold modification (Section 2.1). For the phantom images, a clear 1D-RNAV signal was obtained while weak signal loss was observed in the images, which was most likely caused by the increased FA (60°).

The CV was used to quantify breathing variability. A larger reduction in variability was found for the respiratory period than for the amplitude, which agrees with the work by Lee et al.,[16] who found a reduction of 34% (amplitude) and 73% (period) in 9 lung cancer patients. This difference can be explained by the fact that the breathing period can be adjusted quite simply by providing breath in/out instructions, whereas the VBF is a necessity to perform the desired amplitude motion. For Volunteer 5, no improvement in amplitude was found during the long 4D-MRI acquisition. Figure 4 shows that this volunteer had regular breathing (small SD in end-exhale and end-inhale) during the unguided acquisition, and as a result, no improvement was found. This figure also shows regular breathing for Volunteer 3, but this volunteer had a larger amplitude variability compared with Volunteer 5; therefore, an improvement was found. Sometimes the regular breathing did not feel natural for such a long period; therefore, a more shallow or deeper breath was performed to relax again or to re-align with the guidance waveform, increasing the SD of the individual breathing cycles to be analyzed and therefore increasing the CV.

For free-breathing radiotherapy deliveries, either an ITV or a midposition respiratory motion management strategy may be used to ensure target coverage. Both ITV and midposition assume that motion remains consistent between pretreatment imaging and treatment delivery, whereas, in reality, breathing patterns may change over time,[37] resulting in suboptimal treatments. To maximize dose delivery accuracy during free-breathing treatment deliveries, it is therefore important to maintain stable breathing. VBF reduced the breathing variability and resulted in stable midposition anatomies with median absolute drifts of 0.2 and 0.8 mm. Although VBF did not completely eliminate midposition drift, it reduced drifts in 9 of 10 volunteers. For ITV-based treatment plans, larger motion amplitudes during treatment result in underdosage, whereas smaller motion amplitudes result in overexposure of healthy tissue. VBF on the breathing amplitude can therefore aid the ITV motion management technique. For a midposition-based treatment plan, the van Herk formulation $(M = 2.5\Sigma + 0.67\sqrt{(\sigma_p^2 + \sigma^2 + \sigma_b^2)} - 0.67\sigma_p)$ is typically used to determine the required gross tumor volume–planning target volume margin,[38] where σ_p is the tissue-dependent beam penumbra. Intrafraction drift contributes to both the systematic error (Σ) and the random error (σ), whereas breathing contributes as a random error (σ_b) to the margin. The formula underlines the importance of breathing stability and breathing regularity during midposition-based treatments, to reduce the uncertainties considered in the margin calculation, which can be achieved using VBF. The improvement resulting from VBF shows the potential for ITV and midposition treatment deliveries, as well as for respiratory gating, tumor trailing, and tumor tracking.[17,20] However, a larger amplitude motion (+1.7 mm average) was observed during guided acquisitions with respect to the guidance waveform. A slightly larger increase (+2.2 mm) in CC liver excursion was observed by To et al.,[21] who used an

external surrogate signal for VBF. Training the volunteers could potentially further improved the agreement. The effect of increased motion amplitude can be minimized by incorporating this uncertainty in the treatment plan and performing VBF throughout the full treatment course.

Volunteers were generally able to follow the guidance waveform, with only a small increase in median variability (3%) at the end-exhale locations during the first guided scan. During the first session, the VBF amplitude was changed for the long 4D-MRI acquisition for Volunteer 2, and for Volunteers 4 and 9 the amplitude was changed after the first guided scan to better match their natural breathing. As the amplitude and period were derived from a single 4D-MRI acquisition at the start, it could be that breathing was not representative.

For Volunteer 4, a cranial drift of the midposition anatomy was observed during both long 4D-MRI acquisitions, despite the VBF. Comparing the first and last 4D-MRI subsets, a reduction of 3.3 mm in amplitude was found to be caused primarily by a cranial shift of 4.3 mm of the end-inhale location in the first session. In the second session, again a 4.3-mm cranial shift reduced the amplitude, affecting the $CV^{diff}_{Amplitude}$. This volunteer did not wear prescription glasses during the experiments, and coupled with fatigue toward the end of the session, following the VBF curve was harder for this volunteer. In the future, a simplified GUI for VBF could help in these cases. We demonstrated that healthy volunteers were able to breath regularly for approximately 35 min, which should be sufficient for most treatments. Successful single-fraction gated deliveries (median delivery time of 39 min) with VBF have been demonstrated.[39] Moreover, the eligibility of patients should be investigated, as patients may be poorly conditioned and therefore have difficulty performing the VBF task. A Phase II randomized clinical trial is currently ongoing with audio VBF in Australia, where it is decided before treatment if the breathing regularity increases with VBF.[40]

To ensure physiological plausible VBF, the 1D-RNAV surrogate signal was compared with the 2D-RNAV surrogate signal. The 2D-RNAV derived surrogate signal had, on average, a 20% smaller amplitude compared with the 1D-RNAV signal for the in vivo data, whereas there was an excellent agreement for the phantom validation. This difference is most likely caused by the 4D motion model that is used for obtaining the 2D-RNAV signal. This motion model is a necessity due to nonuniform liver motion over the AP slice locations,[36] whereas this was not present in the phantom validation because of the rigid cylinder used. A significant lower amount of missing data was found for sorted 4D-MRIs using the 1D-RNAV signal compared with the 2D-RNAV signal during VBF. This is most likely caused by the amount of data that was used for sorting the 4D-MRIs, as misregistrations were detected during the process of obtaining the 2D-RNAV signal and excluded for 4D-MRI sorting.[31] The derived 1D-RNAV signal had fewer outliers in detecting motion, likely resulting in less missing data. These findings favor the 1D-RNAV over our 2D-RNAV.

Future research should investigate the applicability of acquiring motion information during MR simulation and applying this as VBF during treatment on the MR-linac, making it possible to personalize the treatment plan based on anatomical motion.

5 | CONCLUSIONS

An SMS-accelerated 4D-MRI acquisition with VBF was developed based on an internal motion navigator. Providing VBF during 4D-MRI acquisitions results in a markedly reduced breathing variability and a more predictable moving anatomy. We compared concurrently acquired 1D and 2D internal navigators used for sorting respiratory-correlated 4D-MRI. Similar performance was found in acquired phantom data, whereas lower amplitude estimates were found with the 2D-RNAV for in vivo data. Fewer missing data in the sorted 4D-MRI was found when the 1D-RNAV signal was used, whereas a larger error was found for the liver–lung interface smoothness.

ACKNOWLEDGMENTS

The authors acknowledge funding by the Dutch Research Council through Project No. 17515 (BREATHE EASY). They acknowledge the research agreements with Elekta AB (Stockholm, Sweden) and Philips Healthcare (Best, The Netherlands). The authors also thank Dr. S. J. Woodings for proofreading the manuscript.

FUNDING INFORMATION

Nederlandse Organisatie voor Wetenschappelijk Onderzoek; Grant/Award No. 17515.

CONFLICT OF INTEREST

Nothing to report.

ORCID

Katrinus Keijnemans https://orcid.org/0000-0002-9335-526X
Pim T. S. Borman https://orcid.org/0000-0003-4153-2241
Bas W. Raaymakers https://orcid.org/0000-0002-8036-6808
Martin F. Fast https://orcid.org/0000-0001-9107-4627

REFERENCES

1. Keall PJ, Mageras GS, Balter JM, et al. The management of respiratory motion in radiation oncology report of AAPM Task Group 76. *Med Phys.* 2006;33:3874-3900. doi:10.1118/1.2349696

2. Korreman S, Persson G, Nygaard D, Brink C, Juhler-Nøttrup T. Respiration-correlated image guidance is the most important radiotherapy motion management strategy for most lung cancer patients. *Int J Radiat Oncol Biol Phys.* 2012;83:1338-1343. doi:10.1016/j.ijrobp.2011.09.010
3. Paulson ES, Tijssen RHN. Motion management. In: Liney G, van der Heide U, eds. *MRI for Radiotherapy: Planning, Delivery, and Response Assessment*. Springer; 2019:107-116.
4. Vedam SS, Keall PJ, Kini VR, Mostafavi H, Shukla HP, Mohan R. Acquiring a four-dimensional computed tomography dataset using an external respiratory signal. *Phys Med Biol.* 2003;48:45-62. doi:10.1088/0031-9155/48/1/304
5. Ford EC, Mageras GS, Yorke E, Ling CC. Respiration-correlated spiral CT: a method of measuring respiratory-induced anatomic motion for radiation treatment planning. *Med Phys.* 2003;30:88-97. doi:10.1118/1.1531177
6. Low DA, Nystrom M, Kalinin E, et al. A method for the reconstruction of four-dimensional synchronized CT scans acquired during free breathing. *Med Phys.* 2003;30:1254-1263. doi:10.1118/1.1576230
7. Keall PJ. Four-dimensional computed tomography imaging and treatment planning. *Semin Radiat Oncol.* 2004;14:81-90. doi:10.1053/j.semradonc.2003.10.006
8. Taguchi K. Temporal resolution and the evaluation of candidate algorithms for four-dimensional CT. *Med Phys.* 2003;30:640-650. doi:10.1118/1.1561286
9. Sonke JJ, Zijp L, Remeijer P, van Herk M. Respiratory correlated cone beam CT. *Med Phys*. 2005;32:1176-1186. doi:10.1118/1.1869074
10. Olsen J, Green O, Kashani R. World's first applicaton of MR-guidance for radiotherapy. *Mo Med.* 2015;112:358-360.
11. Raaymakers BW, Jürgenliemk-Schulz IM, Bol GH, et al. First patients treated with a 1.5 T MRI-Linac: clinical proof of concept of a high-precision, high-field MRI guided radiotherapy treatment. *Phys Med Biol.* 2017;62:L41-L50. doi:10.1088/1361-6560/aa9517
12. Paulson ES, Ahunbay E, Chen X, et al. FourD-MRI driven MR-guided online adaptive radiotherapy for abdominal stereotactic body radiation therapy on a high field MR-Linac: implementation and initial clinical experience. *Clin Transl Radiat Oncol.* 2020;23:72-79. doi:10.1016/j.ctro.2020.05.002
13. van de Lindt TN, Nowee ME, Janssen T, et al. Technical feasibility and clinical evaluation of 4D-MRI guided liver SBRT on the MR-Linac. *Radiother Oncol.* 2022;167:285-291. doi:10.1016/j.radonc.2022.01.009
14. Kim T, Lewis BC, Price A, et al. Direct tumor visual feedback during free breathing in 0.35T MRgRT. *J Appl Clin Med Phys.* 2020;21:241-247. doi:10.1002/acm2.13016
15. van Sörnsen de Koste JR, Palacios MA, Bruynzeel AME, Slotman BJ, Senan S, Lagerwaard FJ. MR-guided gated stereotactic radiation therapy delivery for lung, adrenal, and pancreatic tumors: a geometric analysis. *Int J Radiat Oncol Biol Phys.* 2018;102:858-866. doi:10.1016/j.ijrobp.2018.05.048
16. Lee D, Greer PB, Ludbrook J, et al. Audiovisual biofeedback improves cine–magnetic resonance imaging measured lung tumor motion consistency. *Int J Radiat Oncol Biol Phys.* 2016;94:628-636. doi:10.1016/j.ijrobp.2015.11.017
17. George R, Chung TD, Vedam SS, et al. Audio-visual biofeedback for respiratory-gated radiotherapy: impact of audio instruction and audio-visual biofeedback on respiratory-gated radiotherapy. *Int J Radiat Oncol Biol Phys.* 2006;65:924-933. doi:10.1016/j.ijrobp.2006.02.035
18. Lim S, Park SH, Do Ahn S, et al. Guiding curve based on the normal breathing as monitored by thermocouple for regular breathing. *Med Phys.* 2007;34:4514-4518. doi:10.1118/1.2795829
19. Locklin JK, Yanof J, Luk A, Varro Z, Patriciu A, Wood BJ. Respiratory biofeedback during CT-guided procedures. *J Vasc Interv Radiol.* 2007;18:749-755. doi:10.1016/j.jvir.2007.03.010
20. Pollock S, Lee D, Keall PJ, Kim T. Audiovisual biofeedback improves motion prediction accuracy. *Med Phys.* 2013;40:041705. doi:10.1118/1.4794497
21. To DT,Kim JP, Price RG, Chetty IJ, Glide-Hurst CK. Impact of incorporating visual biofeedback in 4D MRI. *J Appl Clin Med Phys.* 2016;17:128-137. doi:10.1120/jacmp.v17i3.6017
22. Kim T, Pollock S, Lee D, O'Brien R, Keall PJ. Audiovisual biofeedback improves diaphragm motion reproducibility in MRI. *Med Phys.* 2012;39:6921-6928. doi:10.1118/1.4761866
23. Yang J, Yamamoto T, Pollock S, et al. The impact of audiovisual biofeedback on 4D functional and anatomic imaging: results of a lung cancer pilot study. *Radiother Oncol.* 2016;120:267-272. doi:10.1016/j.radonc.2016.05.016
24. Koch N, Liu HH, Starkschall G, et al. Evaluation of internal lung motion for respiratory-gated radiotherapy using MRI: part I—correlating internal lung motion with skin fiducial motion. *Int J Radiat Oncol Biol Phys.* 2004;60:1459-1472. doi:10.1016/j.ijrobp.2004.05.055
25. Liu HH, Koch N, Starkschall G, et al. Evaluation of internal lung motion for respiratory-gated radiotherapy using MRI: part II—margin reduction of internal target volume. *Int J Radiat Oncol Biol Phys.* 2004;60:1473-1483. doi:10.1016/j.ijrobp.2004.05.054
26. Li G, Wei J, Olek D, et al. Direct comparison of respiration-correlated four-dimensional magnetic resonance imaging reconstructed using concurrent internal navigator and external bellows. *Int J Radiat Oncol Biol Phys.* 2017;97:596-605. doi:10.1016/j.ijrobp.2016.11.004
27. Sachs TS, Meyer CH, Hu BS, Kohli J, Nishimura DG, Macovski A. Real-time motion detection in spiral MRI using navigators. *Magn Reson Med.* 1994;32:639-645. doi:10.1002/mrm.1910320513
28. Ehman RL, Felmlee JP. Adaptive technique for high-definition MR imaging of moving structures. *Radiology.* 1989;173:255-263. doi:10.1148/radiology.173.1.2781017
29. Kim JI, Lee H, Wu HG, Chie EK, Kang HC, Park JM. Development of patient-controlled respiratory gating system based on visual guidance for magnetic-resonance image-guided radiation therapy. *Med Phys.* 2017;44:4838-4846. doi:10.1002/mp.12447
30. Stemkens B, Paulson ES, Tijssen RHN. Nuts and bolts of 4D-MRI for radiotherapy. *Phys Med Biol.* 2018;63:21TR01. doi:10.1088/1361-6560/aae56d
31. Keijnemans K, Borman PTS, van Lier ALHMW, Verhoeff JJC, Raaymakers BW, Fast MF. Simultaneous multi-slice accelerated 4D-MRI for radiotherapy guidance. *Phys Med Biol.* 2021;66:095014. doi:10.1088/1361-6560/abf591
32. Hardy CJ, Cline HE. Spatial localization in two dimensions using NMR designer pulses. *J Magn Reson.* 1989;82:647-654. doi:10.1016/0022-2364(89)90230-8
33. Borman PTS, Raaymakers BW, Glitzner M. ReconSocket: a low-latency raw data streaming interface for real-time

MRI-guided radiotherapy. *Phys Med Biol.* 2019;64:185008. doi:10.1088/1361-6560/ab3e99
34. Borman PTS, Tijssen RHN, Bos C, Moonen CTW, Raaymakers BW, Glitzner M. Characterization of imaging latency for real-time MRI-guided radiotherapy. *Phys Med Biol.* 2018;63:155023. doi:10.1088/1361-6560/aad2b7
35. George R, Vedam SS, Chung TD, Ramakrishnan V, Keall PJ. The application of the sinusoidal model to lung cancer patient respiratory motion. *Med Phys.* 2005;32:2850-2861. doi:10.1118/1.2001220
36. Keijnemans K, Borman PTS, Uijtewaal P, Woodhead PL, Raaymakers BW, Fast MF. A hybrid 2D/4D-MRI methodology using simultaneous multislice imaging for radiotherapy guidance. *Med Phys*. 2022;49:6068-6081. doi:10.1002/mp.15802
37. Dhont J, Vandemeulebroucke J, Burghelea M, et al. The long- and short-term variability of breathing induced tumor motion in lung and liver over the course of a radiotherapy treatment. *Radiother Oncol*. 2018;126:339-346. doi:10.1016/j.radonc.2017.09.001
38. van Herk M, Remeijer P, Rasch C, Lebesque JV. The probability of correct target dosage: dose-population histograms for deriving treatment margins in radiotherapy. *Int J Radiat Oncol Biol Phys.* 2000;47:1121-1135. doi:10.1016/S0360-3016(00)00518-6
39. Finazzi T, van Sörnsen de Koste JR, Palacios MA, et al. Delivery of magnetic resonance-guided single-fraction stereotactic lung radiotherapy. *Phys Imaging Radiat Oncol.* 2020;14:17-23. doi:10.1016/j.phro.2020.05.002
40. Pollock S, O'Brien R, Makhija K, et al. Audiovisual biofeedback breathing guidance for lung cancer patients receiving radiotherapy: a multi-institutional phase II randomised clinical trial. *BMC Cancer.* 2015;15:526. doi:10.1186/s12885-015-1483-7

How to cite this article: Keijnemans K, Borman PTS, Raaymakers BW, Fast MF. Effectiveness of visual biofeedback–guided respiratory-correlated 4D-MRI for radiotherapy guidance on the MR-linac. *Magn Reson Med*. 2024;91:297-311. doi: 10.1002/mrm.29857